

基于双 2+1 相移法的高动态范围三维测量

王建华^{1*}, 杨延西², 徐鹏¹, 刘锦涛¹, 张雯¹, 单硕¹, 李泽¹¹青岛理工大学信息与控制工程学院, 山东 青岛 266520;²西安理工大学自动化与信息工程学院, 陕西 西安 710048

摘要 针对基于 2+1 相移法的高反光表面三维测量, 分析了强度饱和条纹图案的傅里叶频谱, 引入了强度饱和条纹的三阶傅里叶级数表达形式, 建立了强度饱和和所致的包裹相位误差模型, 提出了双 2+1 相移法。从精度和效率两方面进行了对比实验: 对比传统的 2+1 相移法和自适应条纹投影的 2+1 相移法, 双 2+1 相移法的相位误差分别降低了 69.9% 和 65.2%; 对比多曝光 2+1 相移法和自适应条纹投影的 2+1 相移法, 双 2+1 相移法的测量效率分别提高了 91.9% 和 63.9%。

关键词 高反光表面; 强度饱和条纹; 相位误差模型; 双 2+1 相移法

中图分类号 TN247

文献标志码 A

DOI: 10.3788/AOS230809

1 引言

条纹投影轮廓术(FPP)具有精度高、速度快、成本低、全场测量和易于实现等优点, 已成为非接触式三维测量的重要研究方向。相位提取精度和效率直接关系到 FPP 的测量精度和效率^[1-3]。单帧条纹的 FPP 通常采用变换法(傅里叶变换、小波变换、S 变换等)提取包裹相位(或称截断相位、相位主值), 再采用空域相位展开方法(枝切法、质量图导向法和最小范数法)得到展开相位(或称连续相位), 但相位提取的精度和鲁棒性不高, 限制了其应用^[4-8]。多帧条纹的 FPP 通常采用相移法提取不同频率的包裹相位, 再采用时域相位展开方法(多频率法、多波长法等)得到连续相位, 其相位提取的精度和鲁棒性很高, 但多幅条纹投影限制了其测量效率与动态测量应用^[9-15]。

Zhang 等^[16]提出的 2+1 相移法可以减少运动引起的相位误差, 将 2+1 相移法与时域相位展开结合, 可以得到 $2f_H + a + 2f_L$ 算法和 $2f_H + a + 2f_M + 2f_L$ 算法(即两幅高频 f_H 条纹, 一幅背景强度 a 图像, 两幅中频 f_M 条纹和两幅低频 f_L 条纹)。然而, 对于各种常见的静态金属、陶瓷、塑料制品等, 测量表面具有局部高反光, 导致采集条纹图案局部强度饱和, 从而造成编码失真, 难以正确提取相位信息, 并最终导致三维重建形貌局部信息缺失等误差^[17-19]。为此, 许多学者提出了解决方法, 这些方法统称为高动态范围(HDR)技术,

可分三类: 1) 多重曝光的技术。Zhang 等^[20]首先提出了多重曝光技术, 从 23 组条纹序列中选择像素强度在该序列都不饱和且在所有条纹序列中强度最大的视为最终结果, 从而构建出用于相位计算的最终一套条纹序列, 该方法的条纹信噪比良好, 但其曝光时间和范围难以量化, 且测量效率较低。Feng 等^[21]根据灰度直方图将被测表面分为几组, 然后估计每组的最佳曝光时间, 最后也提取一套最终条纹序列。该方法得到了量化的曝光时间和范围, 提高了测量效率。但是, 对于灰度不集中的表面, 这种直方图分类方法是不准确的。Jiang 等^[22]提出了一种将曝光时间调整和投影条纹强度调整结合的混合方法, 还开发了一种最佳曝光时间和投影光强度参数的自动选择方法。但是, 该方法相对复杂, 且仍需要大约 6 套条纹序列。上述基于多重曝光技术及其改进技术通常具有良好的图像信噪比, 但曝光次数通常较大, 测量效率不高。2) 自适应条纹投影技术。Waddington 等^[23-24]提出了一种基于条纹最大输入灰度级校正技术的图像饱和和抑制方法。但是, 在测量过暗的低反射区域时, 条纹信噪比降低。Lin 等^[25]根据预采集图像自适应调整投影条纹的像素强度, Chen 等^[26]根据被测表面的反射特性, 采用拟合算法计算最佳投影条纹强度, 上述方法的问题在于当投影条纹强度较低时, 环境光干扰不容忽视, 降低了捕获的条纹图案的信噪比。3) 采用偏振滤光片技术。对于非导电材料, 镜面反射后的反射光是偏振的, 而漫反射后的反射光没有偏振。基于上

收稿日期: 2023-04-13; 修回日期: 2023-05-04; 录用日期: 2023-05-09; 网络首发日期: 2023-06-28

基金项目: 山东省自然科学基金(ZR2021MF024)、国家自然科学基金(62273274)

通信作者: *wangjianhua@qut.edu.cn

述原理, Nayar 等^[27]在相机前面安装了一个偏振器, 并结合颜色信息来分离图像的漫反射区域和镜面反射区域。Salahieh 等^[28]提出了一种多偏振条纹投影系统, 通过选择合适的偏振通道来消除图像饱和度, 提高了条纹对比度。该方法仅适用于抑制高光表面, 对过暗表面反而会降低条纹信噪比, 该方法需要增加硬件成本, 且在使用偏振滤光片前必须调整物体和光路, 操作较为复杂。

针对上述问题, 本文提出了校正强度饱和引入相位误差的双 2+1 相移法。首先, 分析了强度饱和和条纹图案的傅里叶频谱并用高阶傅里叶级数描述了强度饱和和条纹图案, 随后建立了强度饱和引入相位误差模型, 基于该相位误差模型提出了一种双 2+1 相移法, 其原理是通过投影一组相移 π 的附加条纹序列来产生相反的相位误差, 从而融合两相位以减少误差。其次, 回顾了 2+1 相移法、时域相位展开法和三维重建基础理论。然后, 分析了强度饱和和条纹图案的傅里叶频谱并建立了强度饱和引入相位误差模型, 进而提出了双 2+1 相移法。最后, 通过实验证实了所提方法在强度饱和引入相位误差上的校正能力, 并对比了测量效率。

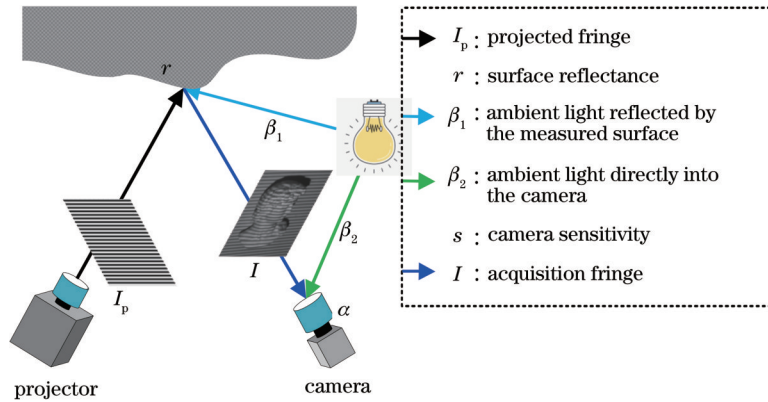


图 1 条纹投影与采集

Fig. 1 Fringe projection and acquisition

2.2 2+1 相移法和三频分层时域相位展开

2+1 相移法得到了包裹相位, 根据 Wang 等^[29]对基于少条纹相位提取算法的噪声抑制能力的对比可知, 2+1 相移法对噪声引入包裹相位误差的抑制能力低于三步相移法和四步相移法, 但其运动引入相位误差相对更小。时域相位展开常用多频法(分层法)和多波长法(外差法), 根据 Zuo 等^[9]和 Wang 等^[30]对分层时域相位展开和外差时域相位展开的可靠性对比可知, 分层时域相位展开的可靠性更高。假设三频和双频分层时域相位展开的条纹图案引入噪声方差和最大条纹频率相同, 因三频分层相位展开的频率比值要小于双频分层时域相位展开, 从而三频分层相位展开的噪声引入相位误差放大倍数更小, 因此, 三频比双频分层时

2 基于 2+1 相移法的条纹投影轮廓术基础原理

2.1 基于 FPP 的条纹投影和采集

计算机生成的投影条纹可以表示为

$$I_p(x_p, y_p) = A(x_p, y_p) + B(x_p, y_p) \cos(2\pi f x_p), \quad (1)$$

式中: (x_p, y_p) 为投影仪的像素坐标。对于 8 bit 灰度图, 为覆盖整个 8 位图像灰度范围, 通常 $A=B=127.5$ 。 f 为条纹频率, $f=1/\lambda$, λ 代表条纹波长, $\lambda=W/T$, T 表示沿投影条纹的 x 轴的周期数, W 表示条纹宽度。

摄像机采集条纹的强度与投影条纹的强度、被测表面反射率、摄像机敏感度(s 为镜头相对孔径的平方与镜头透光率的乘积)和环境光强有关^[20], 如图 1 所示。

$$I(x, y) = sr(x, y) [I_p(x, y) + \beta_1(x, y)] + s\beta_2(x, y) = a(x, y) + b(x, y) \cos \phi(x, y), \quad (2)$$

$$a(x, y) = sr(x, y) [A + \beta_1(x, y)] + s\beta_2(x, y), \quad (3)$$

$$b(x, y) = sr(x, y)B, \quad (4)$$

式中: (x, y) 为摄像机的像素坐标; s 为摄像机敏感度^[20]; r 为物体表面反射率; β_1 表示被测表面反射后的环境光; β_2 表示直接进入摄像机的环境光; a 和 b 代表采集条纹的背景和调制强度; ϕ 是要求解的相位。

域相位展开的可靠性更高。这里采用了三频分层时域相位展开, 因此 2+1 相移法和三频分层时域相位展开结合计算展开相位, 这里简称 $2f_H + a + 2f_M + 2f_L$ 算法。为简化书写, 省略像素坐标后的条纹序列表示为

$$\begin{cases} I_1 = a + b \sin \phi_H, I_2 = a + b \cos \phi_H, I_3 = a \\ I_4 = a + b \sin \phi_M, I_5 = a + b \cos \phi_M \\ I_6 = a + b \sin \phi_L, I_7 = a + b \cos \phi_L \end{cases}, \quad (5)$$

式中: ϕ_H 、 ϕ_M 和 ϕ_L 代表高频、中频和低频条纹的包裹相位。对于分层时域相位展开, 低频条纹周期为 1 (条纹频率为 $1/W$, W 是条纹宽度), 因此低频条纹的展开相位等于其包裹相位。中频和低频条纹的周期数合理选择可以根据 Zhang 等^[31]的最优条纹频率和条纹序列选择, 这里高频、中频和低频条纹的周期数选择 $\{180,$

15, 1}, 即频率为 $\{180/W, 15/W, 1/W\}$ 且 $W=912$ pixel。

基于 2+1 相移法的高频、中频和低频条纹的包裹相位为

$$\begin{cases} \phi_H = \arctan \frac{I_1 - I_3}{I_2 - I_3} \\ \phi_M = \arctan \frac{I_4 - I_3}{I_5 - I_3} \\ \phi_L = \arctan \frac{I_6 - I_3}{I_7 - I_3} \end{cases} \quad (6)$$

展开相位和包裹相位之间满足 $\Phi = \phi + 2k\pi$, k 表示相位折叠级数, 高频、中频和低频条纹的展开相位可以采用下式得到。

$$\begin{cases} \Phi_H = \phi_H + 2\pi \times \text{round} \left[\frac{(f_H/f_M)\Phi_M - \phi_H}{2\pi} \right] \\ \Phi_M = \phi_M + 2\pi \times \text{round} \left[\frac{(f_M/f_L)\Phi_L - \phi_M}{2\pi} \right] \\ \Phi_L = \phi_L \end{cases} \quad (7)$$

2.3 三维几何形貌重建

基于张氏平面标定法可以高精度地获取摄像机的内参 A_C 和外参 $[R_C, T_C]$ 。将投影仪作为逆向摄像机, 通过建立投影仪和摄像机的像素映射, 可以得到投影仪近似采集的标定板图像, 类似于摄像机的平面标定

法得到投影仪的内参 A_P 和外参 $[R_P, T_P]$, 进而建立如下的像素坐标和世界坐标的单应性矩阵:

$$p_C = A_C [R_C, T_C] = \begin{bmatrix} \rho_{11}^C & \rho_{12}^C & \rho_{13}^C & \rho_{14}^C \\ \rho_{21}^C & \rho_{22}^C & \rho_{23}^C & \rho_{24}^C \\ \rho_{31}^C & \rho_{32}^C & \rho_{33}^C & \rho_{34}^C \end{bmatrix}, \quad (8)$$

$$p_P = A_P [R_P, T_P] = \begin{bmatrix} \rho_{11}^P & \rho_{12}^P & \rho_{13}^P & \rho_{14}^P \\ \rho_{21}^P & \rho_{22}^P & \rho_{23}^P & \rho_{24}^P \\ \rho_{31}^P & \rho_{32}^P & \rho_{33}^P & \rho_{34}^P \end{bmatrix} \quad (9)$$

进一步根据展开相位 $\Phi(x, y)$ 得到摄像机像素坐标 (x, y) 对应的投影坐标 x_P , 基于下式重建三维形貌^[32]。

$$x_P = \frac{\Phi(x, y)W}{2\pi T}, \quad (10)$$

$$\begin{bmatrix} x_w \\ y_w \\ z_w \end{bmatrix} = \begin{bmatrix} \rho_{11}^C - x_P \rho_{31}^C & \rho_{12}^C - x_P \rho_{32}^C & \rho_{13}^C - x_P \rho_{33}^C \\ \rho_{21}^C - y_P \rho_{31}^C & \rho_{22}^C - y_P \rho_{32}^C & \rho_{23}^C - y_P \rho_{33}^C \\ \rho_{11}^P - x_P \rho_{31}^P & \rho_{12}^P - x_P \rho_{32}^P & \rho_{13}^P - x_P \rho_{33}^P \end{bmatrix}^{-1} \times \begin{bmatrix} x_P \rho_{34}^C - \rho_{14}^C \\ y_P \rho_{34}^C - \rho_{24}^C \\ x_P \rho_{34}^P - \rho_{14}^P \end{bmatrix}, \quad (11)$$

式中: Φ 是展开相位; T 是条纹周期数。

采集条纹、包裹相位、展开相位和三维点云如图 2 所示。

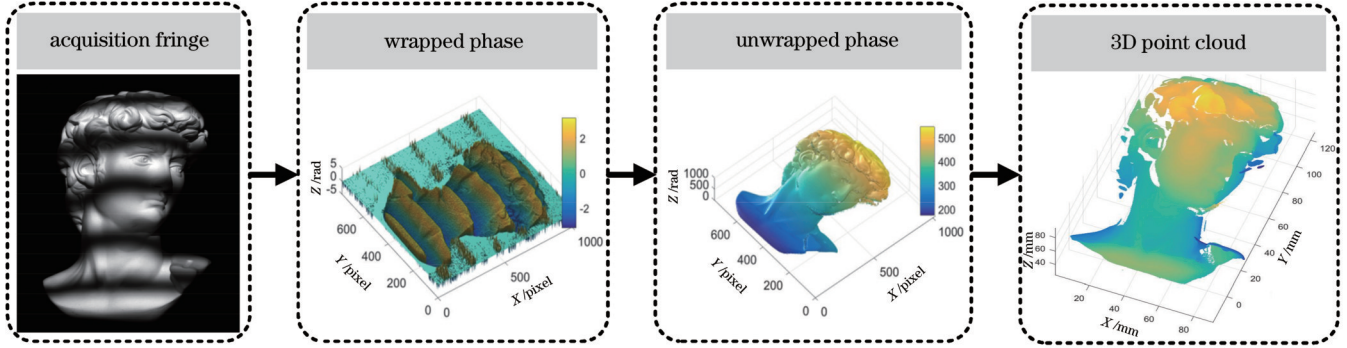


图 2 包裹相位、展开相位和三维点云

Fig. 2 Wrapped phase, unwrapped phase and 3D point cloud

3 所提算法

3.1 强度饱和条纹的傅里叶频谱分析

强度饱和条纹引入了高次谐波分量, 为分析强度饱和的影响, 计算机模拟了强度饱和条纹, 可以表示为

$$I_{k,P} = kI_P = \begin{cases} k[A + B\cos(2\pi fx_P)], & I_{k,P} < 255 \\ 255, & I_{k,P} \geq 255 \end{cases}, \quad (12)$$

式中: I_P 是原始条纹; k 为强度系数, $k > 1$ 时, 条纹发生饱和, 且饱和程度随 k 的增大而增大。计算机模拟时的背景和调制强度为 $A=B=127.5$ 。

图 3 为模拟不同强度系数的条纹及其傅里叶频谱, 零频分量代表背景强度。当强度饱和条纹时, 除了

基频分量, 还有高频分量, 且高频分量随着强度饱和系数的增大而增大。进一步模拟被测物体调制后的条纹图案。模拟物体如图 4(a) 所示, 非强度饱和的条纹及其一行横截面如图 4(b)、(d) 所示, 强度饱和的条纹及其一行横截面如图 4(c)、(e) 所示。图 4(f)、(g) 分别为非饱和条纹频谱与饱和条纹频谱。通过对比看出, 强度饱和条纹进一步产生了高频分量。

因此, 强度饱和条纹可用多阶傅里叶级数表示

$$I = a_0 + \sum_{i=1}^M a_i \cos[i\phi], \quad (13)$$

式中: M 表示 M 阶谐波, $i \in [1, M]$ 。计算机数值模拟时, 包裹相位 $\phi(x, y) = (2\pi fx) \bmod \pi$, \bmod 为取余

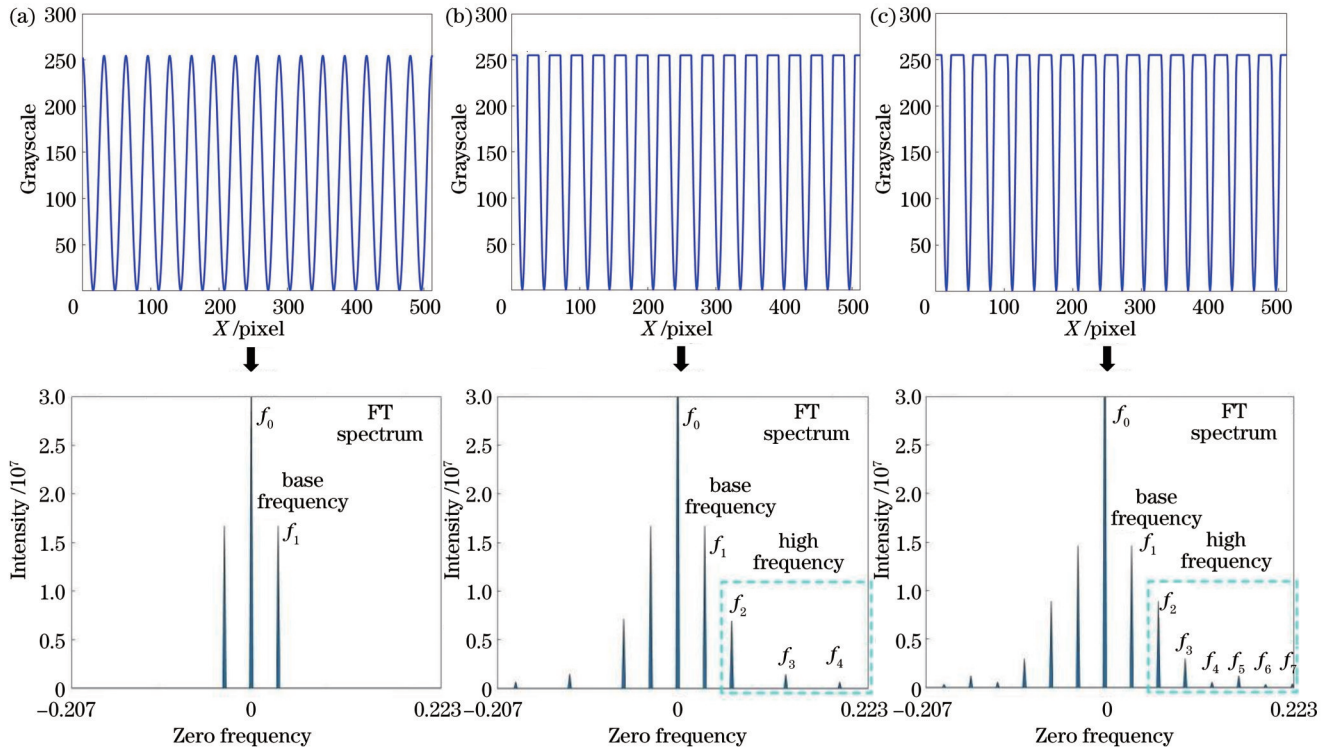


图 3 计算机模拟强度饱和条纹的傅里叶频谱。(a) $k=1$ 的条纹与频谱;(b) $k=2$ 的条纹与频谱;(c) $k=3$ 的条纹与频谱

Fig. 3 Fourier spectrum of computer simulation of intensity saturated fringe. (a) Fringe and spectrum of $k=1$; (b) fringe and spectrum of $k=2$; (c) fringe and spectrum of $k=3$

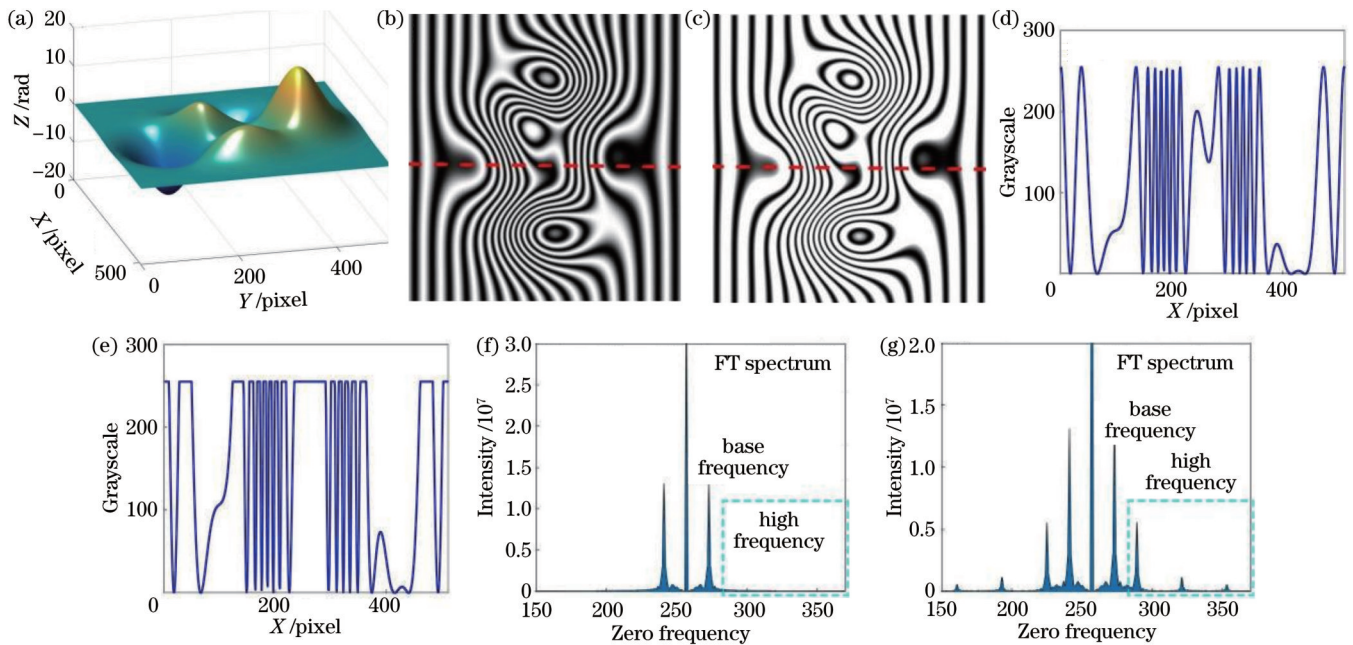


图 4 计算机模拟物体调制的强度饱和条纹的傅里叶频谱。(a)模拟被测面;(b) $k=1$ 的条纹;(c) $k=2$ 的条纹;(d) $k=1$ 的一行像素;(e) $k=2$ 的一行像素;(f) $k=1$ 的频谱;(g) $k=2$ 的频谱

Fig. 4 Fourier spectrum of intensity-saturated fringe modulated by computer-simulated object. (a) Simulated surface; (b) fringe of $k=1$; (c) fringe of $k=2$; (d) a row of pixels of $k=1$; (e) a row of pixels of $k=2$; (f) spectrum of $k=1$; (g) spectrum of $k=2$

算子。

3.2 强度饱和条纹引入包裹相位误差的模型建立

从图 3 和图 4 可以看出,频率 f_3 以上的谐波分量幅值较小,为简化模型,假设频率 f_3 以上的强度饱和引入

谐波分量可以忽略,则强度饱和和条纹模型可以简化为三阶傅里叶级数,即式(13)中的 $M=3$ 。针对 $2+1$ 相移法,强度饱和和条纹简化为三阶傅里叶级数,因此 $2+1$ 相移法的强度饱和和条纹可以表示为

$$\begin{cases} I'_1 = a_0 + \sum_{i=1}^3 a_i \sin(i\phi) \\ I'_2 = a_0 + \sum_{i=1}^3 a_i \cos(i\phi) \\ I'_3 = a_0 \end{cases} \quad (14)$$

强度饱和时,基于 2+1 相移法的实际包裹相位为

$$\phi_R = \arctan \frac{I'_1 - I'_3}{I'_2 - I'_3} = \arctan \frac{a_1 \sin \phi + 2a_2 \sin \phi \cos \phi + 2a_3 \sin \phi \cos^2 \phi + a_3 \sin \phi - 2a_3 \sin^3 \phi}{a_1 \cos \phi + 2a_2 \cos^2 \phi - a_2 + 2a_3 \cos^3 \phi - a_3 \cos \phi - 2a_3 \sin^2 \phi \cos \phi} \quad (15)$$

强度饱和引入的包裹相位误差为

$$\Delta\phi = \arctan(\tan\Delta\phi) = \arctan\left[\tan(\phi_R - \phi_1)\right] = \arctan \frac{\tan \phi_R - \tan \phi_1}{1 + \tan \phi_R \tan \phi_1}, \quad (16)$$

式中: ϕ_1 为理想包裹相位, $\phi_1 = \arctan(\sin \phi / \cos \phi)$; ϕ_R 表示实际包裹相位。

由式(16)可以进一步得到

$$\begin{aligned} \Delta\phi &= \arctan \frac{\frac{a_1 \sin \phi + 2a_2 \sin \phi \cos \phi + 2a_3 \sin \phi \cos^2 \phi + a_3 \sin \phi - 2a_3 \sin^3 \phi}{a_1 \cos \phi + 2a_2 \cos^2 \phi - a_2 + 2a_3 \cos^3 \phi - a_3 \cos \phi - 2a_3 \sin^2 \phi \cos \phi} - \frac{\sin \phi}{\cos \phi}}{1 + \frac{a_1 \sin \phi + 2a_2 \sin \phi \cos \phi + 2a_3 \sin \phi \cos^2 \phi + a_3 \sin \phi - 2a_3 \sin^3 \phi}{a_1 \cos \phi + 2a_2 \cos^2 \phi - a_2 + 2a_3 \cos^3 \phi - a_3 \cos \phi - 2a_3 \sin^2 \phi \cos \phi} \times \frac{\sin \phi}{\cos \phi}} \\ &= \arctan \left(\frac{a_1 \sin \phi \cos \phi + 2a_2 \sin \phi \cos^2 \phi + 2a_3 \sin \phi \cos^3 \phi + a_3 \sin \phi \cos \phi - 2a_3 \sin^3 \phi \cos \phi}{a_1 \sin^2 \phi + 2a_2 \sin^2 \phi \cos \phi + 2a_3 \sin^2 \phi \cos^2 \phi + a_3 \sin^2 \phi - 2a_3 \sin^4 \phi} \right. \\ &\quad \left. - \frac{a_1 \sin \phi \cos \phi - 2a_2 \sin \phi \cos^2 \phi + a_2 \sin \phi - 2a_3 \sin \phi \cos^3 \phi + a_3 \sin \phi \cos \phi + 2a_3 \sin^3 \phi \cos \phi}{a_1 \cos^2 \phi + 2a_2 \cos^3 \phi - a_2 \cos \phi + 2a_3 \cos^4 \phi - a_3 \cos^2 \phi - 2a_3 \sin^2 \phi \cos^2 \phi} \right) \\ &= \arctan \frac{a_2 \sin \phi + 2a_3 \sin \phi \cos \phi}{a_1 + 2a_2 \cos \phi - a_2 \cos \phi + 2a_3 \cos^2 \phi + a_3 \sin^2 \phi - a_3 \cos^2 \phi - 2a_3 \sin^4 \phi - 2a_3 \sin^2 \phi \cos^2 \phi} \\ &= \arctan \frac{a_2 \sin \phi + 2a_3 \sin \phi \cos \phi}{a_1 + a_2 \cos \phi + a_3 - 2a_3 \sin^2 \phi} = \arctan \frac{a_2 \sin \phi + a_3 \sin 2\phi}{a_1 + a_2 \cos \phi + a_3 \cos 2\phi} \quad (17) \end{aligned}$$

如图 3 和 4 所示,强度饱和条纹的三阶傅里叶级数中, $a_1 \gg a_2 \gg a_3$,因此,式(17)的分母项可以简写为 a_1 。同时,式(17)的分母项也远大于分子项,所以

$$\begin{aligned} \Delta\phi &= \arctan \frac{a_2 \sin \phi + a_3 \sin 2\phi}{a_1 + a_2 \cos \phi + a_3 \cos 2\phi} \approx \arctan \frac{a_2 \sin \phi + a_3 \sin 2\phi}{a_1} \approx \frac{a_2 \sin \phi + a_3 \sin 2\phi}{a_1} \\ &= \frac{a_2}{a_1} \sin \phi + \frac{a_3}{a_1} \sin 2\phi = k_1 \sin \phi + k_2 \sin 2\phi, \quad (18) \end{aligned}$$

式中: $k_1 = a_2/a_1, k_2 = a_3/a_1, k_1 \gg k_2$ 。

式(18)为强度饱和导致的包裹相位误差模型,且常数 $k_1 \gg k_2$,因此模型可以近似为

$$\Delta\phi \cong k_1 \sin \phi. \quad (19)$$

3.3 基于双 2+1 相移法的强度饱和和条纹引入包裹相位误差的补偿

基于强度饱和导致的包裹相位误差模型,如果额外一套 2+1 相移条纹可以产生相反包裹相位误差,则可以融合两套 2+1 相移条纹的包裹相位,从而校正包裹相位误差。额外一套 2+1 相移条纹的包裹相位误差为

$$\Delta\phi_A \cong -k_1 \sin \phi = k_1 \sin(\phi + \pi). \quad (20)$$

从式(20)可以看出,额外一套 2+1 相移条纹的相位差为 π ,因此额外一套 2+1 相移条纹可以表示为

$$\begin{cases} I_1^A = a - b \sin \phi_H^A \\ I_2^A = a - b \cos \phi_H^A \\ I_3^A = I_3 = a \end{cases} \quad (21)$$

根据等式(21)可以看出,额外一套 2+1 相移条纹的第三幅图像即为原始一套 2+1 相移条纹的第三幅图像,因此额外一套 2+1 相移条纹实际仅需增加 2 幅条纹。针对 $2f_H + a + 2f_M + 2f_L$ 算法,额外条纹仅增加了 6 幅条纹,可以表示为

$$\begin{cases} I_1^A = a + b \sin \phi_H^A, I_2^A = a + b \cos \phi_H^A \\ I_3^A = a + b \sin \phi_M^A, I_4^A = a + b \cos \phi_M^A \\ I_5^A = a + b \sin \phi_L^A, I_6^A = a + b \cos \phi_L^A \end{cases} \quad (22)$$

基于 2+1 相移法的额外条纹的高频、中频和低频条纹的包裹相位为

$$\begin{cases} \phi_H^\Delta = \arctan \frac{I_1^\Delta - I_3}{I_2^\Delta - I_3} \\ \phi_M^\Delta = \arctan \frac{I_3^\Delta - I_3}{I_4^\Delta - I_3} \\ \phi_L^\Delta = \arctan \frac{I_5^\Delta - I_3}{I_6^\Delta - I_3} \end{cases} \quad (23)$$

额外条纹的高频、中频和低频条纹的展开相位为

$$\begin{cases} \Phi_H^\Delta = \phi_H^\Delta + 2\pi \times \text{round} \left[\frac{(f_H/f_M)\Phi_M^\Delta - \phi_H^\Delta}{2\pi} \right] \\ \Phi_M^\Delta = \phi_M^\Delta + 2\pi \times \text{round} \left[\frac{(f_M/f_L)\Phi_L^\Delta - \phi_M^\Delta}{2\pi} \right] \\ \Phi_L^\Delta = \phi_L^\Delta \end{cases} \quad (24)$$

融合原始和额外的高频条纹展开相位,得到最终展开相位为

$$\Phi_H^F = \frac{\Phi_H + \Phi_H^\Delta}{2} \quad (25)$$

4 实 验

三维测量系统包括数字投影仪(DLP LightCraft 4500,分辨率为912 pixel×1140 pixel)、摄像机(MER-131-210U3M,最大分辨率为1280 pixel×1024 pixel)和计算机。高频、中频和低频条纹的周期数选择{180, 15, 1},即频率为{180/W, 15/W, 1/W}且W=912 pixel。

4.1 所提方法的有效性实验

复杂金属件如图5(a)所示,一幅高频采集条纹如图5(b)所示,因复杂金属件的多处镜面反射,产生多处局部强度饱和,为了不影响图像清晰度,在图5(b)中仅标记了6处局部饱和位置,其他局部饱和位置未标记。图5(c)和图5(d)分别为传统算法和所提方法获得的复杂金属件的展开相位,可以看出,图5(c)中存在多处强度饱和引入相位误差,而图5(d)相对应的强度饱和引入相位误差显著减少甚至消失。为突出对比,对图5(c)和5(d)的局部进行放大并提取图5(c)和5(d)的第350和第400行的局部展开相位进行对比,结果如图5(e)所示。传统方法存在高光反射导致的相位误差,所提方法可以有效地减小高光反射导致的相位误差,实验证实了所提方法的有效性。

4.2 所提方法与现有方法的精度对比

上述实验证实了所提方法的有效性,为进一步证实所提方法相较于现有方法的优势,将所提方法与自适应条纹投影方法和多曝光方法进行了三维重建精度

对比,结果如图6所示。图6(a)为基于传统方法的高频条纹图案、中频条纹图案和低频条纹图案,图6(b)为多曝光方法提取的高频条纹图案、中频条纹图案和低频条纹图案。通过对比图6(a)和图6(b)可以看出,图6(b)的强度饱和得到了显著抑制。图6(c)为自适应条纹投影方法的自适应强度模板、自适应投影条纹和自适应条纹投影后的采集条纹。图6(d)为采用传统方法获得的展开相位,可以看出,在高反射表面上存在大量的相位缺失。图6(e)为通过多曝光方法(23次曝光)获得的展开相位,可以看出,足够多的曝光次数和范围通常可以获得令人满意的结果。图6(f)为通过自适应条纹投影法获得的展开相位,通过对比图6(d)和图6(f)可以看出,自适应条纹投影法仍然有效,但正如理论分析中所描述的,自适应投影强度模板的准确度受到两个方面的限制:1)摄像机图像和投影仪图像之间的像素映射误差;2)摄像机和投影仪的灰度范围所限。图6(g)为通过所提方法获得的展开相位,对比图6(e)和图6(g)可以看出,所提方法提取的展开相位接近于多曝光方法(23次曝光),比传统方法和自适应条纹投影方法要好得多。

为实现定量对比,以多曝光方法(23次曝光)提取的展开相位作为真实值,分别计算传统方法、自适应条纹投影方法和所提方法的均方根误差(RMSE)。RMSE比较结果如表1所示,所提方法的RMSE比传统方法低69.92%,比自适应条纹投影方法低65.2%。

4.3 所提方法与现有方法的测量效率对比

不同算法难易程度和运行速度接近,因此在相同投影和采集速度时,三维重建效率主要取决于所需条纹的数量。传统方法($2f_H+a+2f_M+2f_L$ 算法)的条纹数量为7,多曝光法(23次曝光)的条纹数量为 $7 \times 23 = 161$,自适应投影条纹法的条纹数量为 $7 \times 3 + 15 = 36$ (工作中采用15幅附加图像用于估计相机图像中的最佳投影像素强度。两组条纹序列(水平条纹和垂直条纹)用于建立投影仪和相机之间的像素映射。最后一组自适应条纹序列用于最终相位计算),所提方法的条纹数量为 $7+6=13$ 。不同算法的条纹数量对比如表2所示,相较于多曝光法和自适应条纹投影法,所提方法的测量效率分别提高了91.9%和63.9%。

5 结 论

对于2+1相移法和三频分层时域相位展开结合的 $2f_H+a+2f_M+2f_L$ 算法,金属、塑料和陶瓷等高反射

表1 RMSE对比

Table 1 RMSE comparison

Item	Traditional method	Adaptive fringe projection method	Proposed method
RMSE /rad (23 exposures as true value)	1.5934	1.3772	0.4793

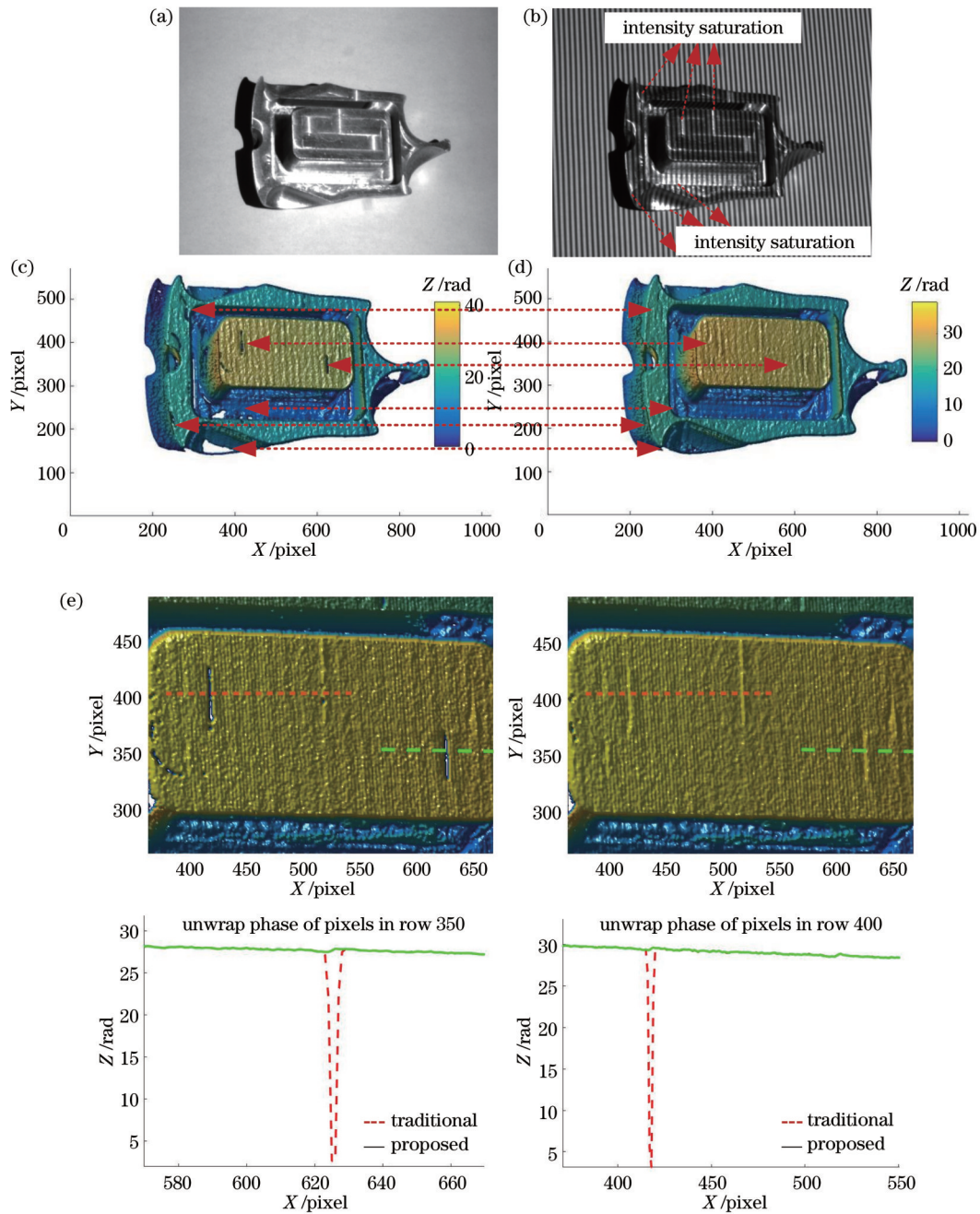


图 5 复杂金属件表面的实验结果对比。(a)复杂金属件;(b)复杂金属件的高频采集条纹;(c)基于传统方法的展开相位;(d)基于所提方法的展开相位;(e)局部放大对比以及一行像素的展开相位对比

Fig. 5 Comparison of experimental results on the surface of complex metal part. (a) Complex metal part; (b) high-frequency acquired fringe on complex metal part; (c) unwrapped phase based on traditional method; (d) unwrapped phase based on the proposed method; (e) local magnification comparison and unwrapped phase comparison of a row of pixels

表面会导致条纹图像强度饱和,从而导致编码失真,进而引入相位误差。现有的多曝光方法测量效率低,曝光时间和曝光范围难以量化。自适应条纹投影方法受到摄像机动态范围以及投影仪与相机图像之间的像素匹配精度的限制,为此,本文提出了双 $2+1$ 相移法。首先,基于对强度饱和条纹图案的傅里叶频谱分析,将强度饱和条纹图案近似用三阶傅里叶级数表示。然后,建立了强度饱和所致的包裹相位误差模型,基于该

模型,投影了额外的相移量为 π 的条纹序列以生成相反的包裹相位误差,并简称为双 $2+1$ 相移法。最后,融合原始条纹序列和额外条纹序列的相位,从而降低了强度饱和引入相位误差。实验证实,所提方法的强度饱和引入相位误差与多曝光方法(23次曝光)相近,但比传统方法和自适应条纹投影法小得多。此外,所提方法的条纹数量明显少于自适应条纹投影法和多曝光法,因此具有很高的测量效率。

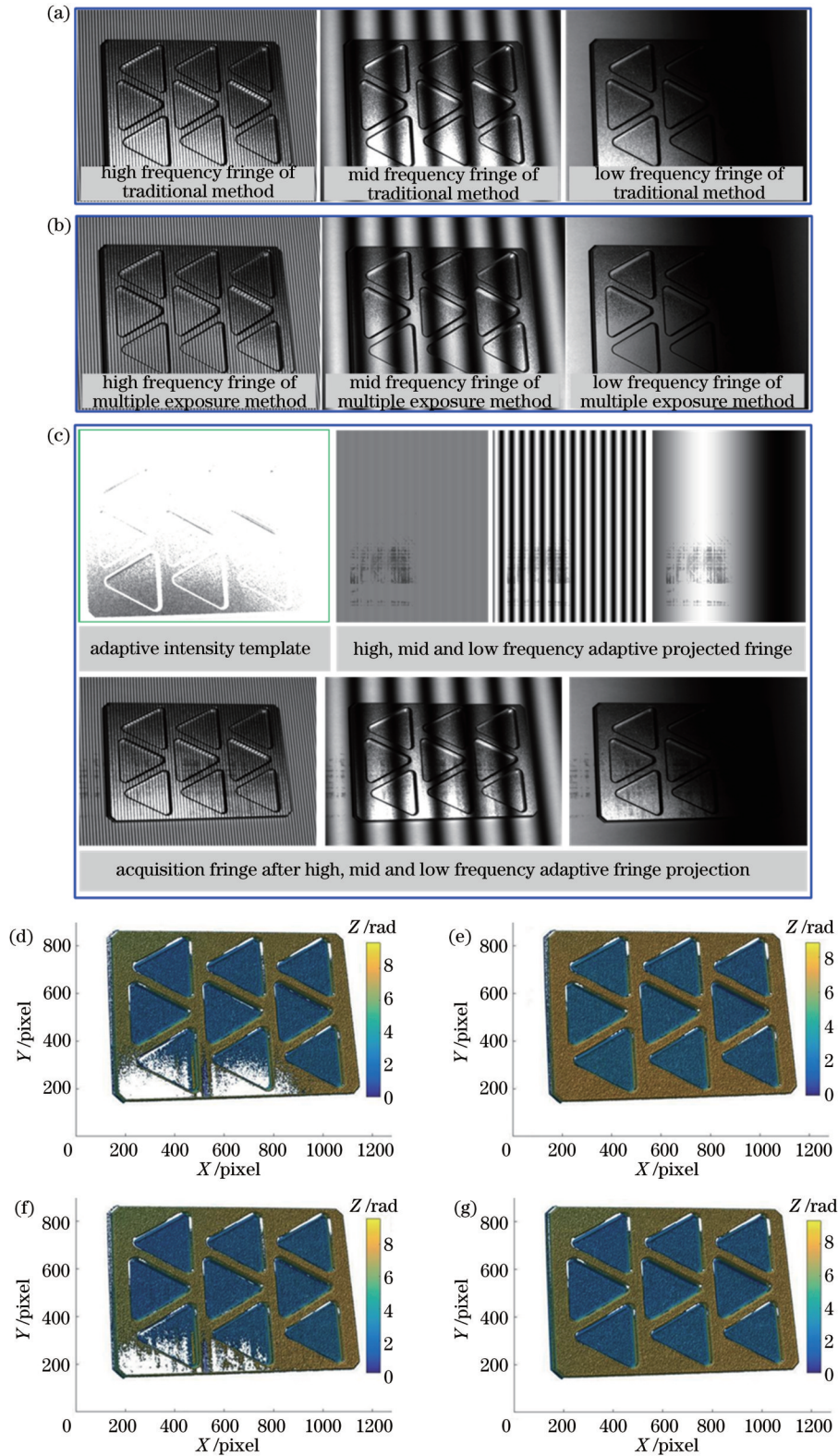


图 6 所提方法与现有方法的实验结果对比。(a)基于传统方法的采集条纹;(b)基于多曝光方法(23次曝光)提取的最优采集条纹;(c)自适应条纹投影方法的自适应强度模板、自适应投影条纹和自适应投影条纹后的采集条纹;(d)基于传统方法的展开相位;(e)基于多曝光法(23次曝光)的展开相位;(f)基于自适应条纹投影方法的展开相位;(g)基于所提方法的展开相位

Fig. 6 Comparison of experimental results of the proposed and traditional methods. (a) Acquired fringe based on traditional method; (b) extracted optimal acquired fringe based on multi-exposure method (23 exposures); (c) adaptive intensity template, adaptive projected fringe, and acquired fringe after adaptive projected fringe for adaptive fringe projection method; (d) unwrapped phase based on traditional method; (e) unwrapped phase based on multi-exposure method (23 exposures); (f) unwrapped phase based on adaptive fringe projection method; (g) unwrapped phase based on the proposed method

表 2 不同方法的条纹数量对比

Table 2 Comparison of the number of fringes of different methods

Item	Traditional method	Multi-exposure method (23 exposures)	Adaptive fringe projection method	Proposed method
Number of fringes	7	161	36	13

参 考 文 献

- [1] Zuo C, Qian J M, Feng S J, et al. Deep learning in optical metrology: a review[J]. *Light: Science & Applications*, 2022, 11: 39.
- [2] 李付谦, 陈文静. 正交光栅相移轮廓术的相位误差分析及其校正[J]. *光学学报*, 2021, 41(14): 1412002.
Li F Q, Chen W J. Phase error analysis and correction for phase shifting profilometry using crossed grating[J]. *Acta Optica Sinica*, 2021, 41(14): 1412002.
- [3] 汪俊霖, 张启灿, 吴周杰. 基于分段阶梯相位编码的三维形貌测量方法[J]. *激光与光电子学进展*, 2022, 59(14): 1415012.
Wang J L, Zhang Q C, Wu Z J. Three-dimensional shape measurement method based on segmented step phase coding[J]. *Laser & Optoelectronics Progress*, 2022, 59(14): 1415012.
- [4] 陆丽莲, 吴周杰, 张启灿. 基于错位格雷码的动态三维形貌测量方法[J]. *光学学报*, 2022, 42(5): 0512005.
Lu L L, Wu Z J, Zhang Q C. Dynamic three-dimensional shape measurement method based on misaligned gray code[J]. *Acta Optica Sinica*, 2022, 42(5): 0512005.
- [5] 严飞, 祁健, 刘银萍, 等. 一种二值编码条纹聚焦投影的三维测量方法[J]. *光学学报*, 2022, 42(22): 2212002.
Yan F, Qi J, Liu Y P, et al. Three-dimensional measurement method of binary coded fringe focusing projection[J]. *Acta Optica Sinica*, 2022, 42(22): 2212002.
- [6] Zuo C, Tao T Y, Feng S J, et al. Micro Fourier Transform Profilometry (μ FTP): 3D shape measurement at 10, 000 frames per second[J]. *Optics and Lasers in Engineering*, 2018, 102: 70-91.
- [7] Yan L P, Zhang H Y, Zhang R, et al. A robust phase unwrapping algorithm based on reliability mask and weighted minimum least-squares method[J]. *Optics and Lasers in Engineering*, 2019, 112: 39-45.
- [8] 吴双卿, 张引, 张三元, 等. 傅里叶变换轮廓术物体三维形貌测量的系统分析及其坐标校准方法[J]. *光学学报*, 2009, 29(10): 2780-2785.
Wu S Q, Zhang Y, Zhang S Y, et al. Analysis of three-dimensional measurement system and the coordinates calibration in Fourier transform profilometry[J]. *Acta Optica Sinica*, 2009, 29(10): 2780-2785.
- [9] Zuo C, Huang L, Zhang M L, et al. Temporal phase unwrapping algorithms for fringe projection profilometry: a comparative review[J]. *Optics and Lasers in Engineering*, 2016, 85: 84-103.
- [10] Liu Z P, Zibley P C, Zhang S. Motion-induced error compensation for phase shifting profilometry[J]. *Optics Express*, 2018, 26(10): 12632-12637.
- [11] Wang J H, Yang Y X. 3D surface reconstruction scheme for dynamic objects: principle and implementation[J]. *Measurement*, 2022, 201: 111718.
- [12] Feng S J, Zuo C, Hu Y, et al. Deep-learning-based fringe-pattern analysis with uncertainty estimation[J]. *Optica*, 2021, 8(12): 1507-1510.
- [13] Feng S J, Zuo C, Tao T Y, et al. Robust dynamic 3-D measurements with motion-compensated phase-shifting profilometry[J]. *Optics and Lasers in Engineering*, 2018, 103: 127-138.
- [14] Lu L, Yin Y K, Su Z L, et al. General model for phase shifting profilometry with an object in motion[J]. *Applied Optics*, 2018, 57(36): 10364-10369.
- [15] Lu L, Jia Z Y, Luan Y S, et al. Reconstruction of isolated moving objects with high 3D frame rate based on phase shifting profilometry[J]. *Optics Communications*, 2019, 438: 61-66.
- [16] Zhang S, Yau S T. High-speed three-dimensional shape measurement system using a modified two-plus-one phase-shifting algorithm[J]. *Optical Engineering*, 2007, 46(11): 113603.
- [17] 李乾, 薛俊鹏, 张启灿, 等. 利用相机响应曲线实现高反光元件三维形貌测量[J]. *光学学报*, 2022, 42(7): 0712001.
Li Q, Xue J P, Zhang Q C, et al. Three dimensional shape measurement of high reflective elements using camera response curve[J]. *Acta Optica Sinica*, 2022, 42(7): 0712001.
- [18] 詹瑜, 胡丹, 刘凯. 面向高反光区域的自适应结构光[J]. *光学学报*, 2022, 42(16): 1612001.
Zhan Y, Hu D, Liu K. Adaptive structured light for high-reflective areas[J]. *Acta Optica Sinica*, 2022, 42(16): 1612001.
- [19] 冯维, 汤少靖, 赵晓冬, 等. 基于自适应条纹的高反光表面三维形貌测量方法[J]. *光学学报*, 2020, 40(5): 0512003.
Feng W, Tang S J, Zhao X D, et al. Three-dimensional shape measurement method of high-reflective surfaces based on adaptive fringe-pattern[J]. *Acta Optica Sinica*, 2020, 40(5): 0512003.
- [20] Zhang S, Yau S T. High dynamic range scanning technique[J]. *Optical Engineering*, 2009, 48(3): 033604.
- [21] Feng S J, Zhang Y Z, Chen Q, et al. General solution for high dynamic range three-dimensional shape measurement using the fringe projection technique[J]. *Optics and Lasers in Engineering*, 2014, 59: 56-71.
- [22] Jiang H Z, Zhao H J, Li X D. High dynamic range fringe acquisition: a novel 3-D scanning technique for high-reflective surfaces[J]. *Optics and Lasers in Engineering*, 2012, 50(10): 1484-1493.
- [23] Waddington C, Kofman J. Analysis of measurement sensitivity to illuminance and fringe-pattern gray levels for fringe-pattern projection adaptive to ambient lighting[J]. *Optics and Lasers in Engineering*, 2010, 48(2): 251-256.
- [24] Waddington C J, Kofman J D. Modified sinusoidal fringe-pattern projection for variable illuminance in phase-shifting three-dimensional surface-shape metrology[J]. *Optical Engineering*, 2014, 53(8): 084109.
- [25] Lin H, Gao J A, Mei Q, et al. Adaptive digital fringe projection technique for high dynamic range three-dimensional shape measurement[J]. *Optics Express*, 2016, 24(7): 7703-7718.
- [26] Chen C, Gao N, Wang X J, et al. Adaptive projection intensity adjustment for avoiding saturation in three-dimensional shape measurement[J]. *Optics Communications*, 2018, 410: 694-702.
- [27] Nayar S K, Fang X S, Boulton T. Separation of reflection components using color and polarization[J]. *International Journal of Computer Vision*, 1997, 21(3): 163-186.
- [28] Salahieh B, Chen Z Y, Rodriguez J J, et al. Multi-polarization fringe projection imaging for high dynamic range objects[J]. *Optics Express*, 2014, 22(8): 10064-10071.
- [29] Wang J H, Yang Y X, Xu P, et al. Noise-induced phase error comparison in multi-frequency phase-shifting profilometry based on few fringes[J]. *Optics & Laser Technology*, 2023, 159: 109034.
- [30] Wang J H, Yang Y X. Phase extraction accuracy comparison based on multi-frequency phase-shifting method in fringe

- projection profilometry[J]. *Measurement*, 2022, 199: 111525.
- [31] Zhang M L, Chen Q A, Tao T Y, et al. Robust and efficient multi-frequency temporal phase unwrapping: optimal fringe frequency and pattern sequence selection[J]. *Optics Express*, 2017, 25(17): 20381-20399.
- [32] Feng S J, Zuo C, Zhang L, et al. Calibration of fringe projection profilometry: a comparative review[J]. *Optics and Lasers in Engineering*, 2021, 143: 106622.

High Dynamic Range 3D Measurement Based on Double 2+1 Phase-Shifting Method

Wang Jianhua^{1*}, Yang Yanxi², Xu Peng¹, Liu Jintao¹, Zhang Wen¹, Shan Shuo¹, Li Ze¹

¹*School of Information and Control Engineering, Qingdao University of Technology, Qingdao 266520, Shandong, China;*

²*School of Automation and Information Engineering, Xi'an University of Technology, Xi'an 710048, Shaanxi, China*

Abstract

Objective The phase-shifting method can extract the phase with high resolution, high precision, and high robustness. However, since the number of fringe patterns is generally three or more, it is sensitive to positional movement. The 2+1 phase-shifting method can reduce the phase error caused by motion. However, the local specular reflection of the measured object causes local intensity saturation, which leads to phase error. Although the multi-exposure method can extract fringe patterns with a better signal-to-noise ratio (SNR), it is difficult to quantify the exposure time and range. In addition, the number of fringe patterns is huge, and the measurement efficiency is low. The adaptive fringe projection method adaptively adjusts the projected pixel intensity according to the pre-acquired image, but its ability to correct the phase error is limited by the following two aspects. One is the pixel-matching error between the camera and the projector, and the other is the limitation of the grayscale range of the camera and projector. The polarization method has a great suppression effect on specular reflection, but it reduces the SNR on low-reflection surfaces. In addition, the adjustment of the optical path is complicated. For the three-dimensional (3D) measurement of highly reflective objects based on the 2+1 phase-shifting method, a novel double 2+1 phase-shifting method is proposed, which can not only correct the saturation-induced wrapped phase error but also has a higher measurement efficiency.

Methods First, the computer simulates the intensity-saturated fringe pattern. When the fringe intensity is saturated, there are high-frequency components in addition to the fundamental frequency component, and the high-frequency components increase with the increase in the intensity saturation coefficient. Therefore, the intensity-saturated fringe pattern can be expressed as a high-order Fourier series. Second, based on the analysis of the Fourier spectrum, the intensity-saturated fringe pattern can be approximately represented by a third-order Fourier series. Third, we calculate the ideal wrapped phase and the actual wrapped phase based on the 2+1 phase-shifting method. We subtract the ideal wrapped phase from the actual wrapped phase and simplify the phase difference according to the Fourier spectrum to establish a saturation-induced wrapped phase error model. From the saturation-induced wrapped phase error model, it can be seen that the 2+1 phase-shifting method contains a saturation-induced wrapped phase error of one time the fundamental frequency. Fourth, based on the above model, the opposite wrapped phase error can be obtained by doing a π phase shift to the original 2+1 phase-shifting fringes. Since the background image (the variable a in Eq. (5)) does not require a π phase shift, the additional fringe sequence is one less than the original fringe sequence. Finally, an additional fringe sequence with a phase shift of π is projected to generate the opposite wrapped phase error. The phase unwrapping adopts three-frequency hierarchical temporal phase unwrapping, and we reduce the saturation-induced wrapped phase error by fusing the unwrapped phases of the original fringe sequence and the additional fringe sequence.

Results and Discussions The multi-exposure method can obtain a high-precision unwrapped phase with enough exposure time and a wide exposure time range. The unwrapped phase extracted by the proposed method is close to the multi-exposure method, which is better than the traditional method and the adaptive fringe projection method (Fig. 6). We use the unwrapped phase extracted by the multi-exposure method (23 exposures) as the ground truth and calculate the root mean square error (RMSE) of the traditional method, the adaptive fringe projection method, and the proposed method, respectively. The RMSE of the proposed method is 69.92% lower than the traditional method and 65.2% lower than the

adaptive fringe projection method (Table 1). Since the computational cost of each algorithm is similar, the measurement efficiency mainly depends on the number of fringes (Table 2). The number of fringes using the traditional method is 7, the number of fringes using the multi-exposure method (23 exposures) is $7 \times 23 = 161$, and that of fringes using the adaptive projection fringe method is $7 \times 3 + 15 = 36$. In contrast, the number of fringes using the proposed method is $7 + 6 = 13$. Compared with that of the multi-exposure method and the adaptive fringe projection method, the measurement efficiency of the proposed method is increased by 91.9% and 63.9%, respectively.

Conclusions The 2+1 phase-shifting method has good performance in suppressing motion errors. However, highly reflective surfaces such as metals, plastics, and ceramics can cause intensity saturation of the fringe pattern, resulting in phase extraction errors. To this end, we propose a new saturation-induced wrapped phase error model of the 2+1 phase-shifting method. Based on the above saturation-induced wrapped phase error model, an efficient and high-precision double 2+1 phase-shifting method for reconstructing strongly reflective surfaces is proposed. Compared with the traditional 2+1 phase-shifting method and 2+1 phase-shifting method of adaptive fringe projection, the proposed method greatly reduces the saturation-induced phase error. Compared with the 2+1 phase-shifting method of adaptive fringe projection and multi-exposure 2+1 phase-shifting method, the proposed method requires fewer additional fringes and thus has higher measurement efficiency. Therefore, the proposed method has potential applications in the 3D reconstruction of highly reflective surfaces.

Key words highly reflective surfaces; fringe intensity saturation; phase error model; double 2+1 phase-shifting method